Numerical Simulations of the Boundary Layer Jet off the Southeastern Coast of China

YU DU

Laboratory for Climate and Ocean-Atmosphere Studies, Department of Atmospheric and Oceanic Sciences, School of Physics, Peking University, Beijing, China

YI-LENG CHEN

Department of Atmospheric Sciences, School of Ocean and Earth Science and Technology, University of Hawai'i at Mānoa, Honolulu, Hawaii

QINGHONG ZHANG

Laboratory for Climate and Ocean-Atmosphere Studies, Department of Atmospheric and Oceanic Sciences, School of Physics, Peking University, Beijing, China

(Manuscript received 17 October 2014, in final form 10 December 2014)

ABSTRACT

A strong coastal boundary layer jet (CBLJ) (~8 m s^{-1}) off the southeastern coast of China (around 28°N, 122°E) is found from the July 2006–11 hourly model data simulated by the Advanced Research Weather Research and Forecasting Model (WRF-ARW) with a 9-km horizontal grid. The southerly CBLJ has a jet core at the 925-hPa level, located along the western periphery of the west Pacific subtropical high (WPSH). The CBLJ is mainly contributed by large-scale enhancement by diurnal forcing and orographic effects by the coastal terrain along the southeastern China coast and the terrain of Taiwan.

Although the geostrophic winds offshore are faster in the afternoon due to the larger east–west pressure gradient caused by land surface heating over the China plain, the CBLJ has a nocturnal (~0200 LST) maximum. In the afternoon hours, easterly ageostrophic winds driven by differential land–sea thermal heating develop at low levels. After sunset, with the disappearance of land surface heating, the ageostrophic winds offshore veer southward by the Coriolis force and combine with the southerly geostrophic flow resulting in a nocturnal maximum in the CBLJ. Furthermore, from two model sensitivity experiments (NoTW and LowFJ), it is apparent that the terrain of Taiwan and Fujian exerts a secondary influence (1–2 m s^{-1}) on the strength of the CBLJ. The orographic blocking by the terrain of Taiwan and Fujian is more significant with a larger (~1 m s^{-1}) southerly wind component north of the Taiwan Strait at night than in the afternoon hours.

1. Introduction

Boundary layer jets (BLJs), which are one type of low-level jet (LLJ) [below 1 km; Du et al. (2014)], frequently occur next to a large mountain range or in regions with land–sea thermal contrast (Stensrud 1996; Rife et al. 2010). In addition to boundary layer jets east of the Rocky Mountains over the U.S. Great Plains (e.g., Bonner 1968; Blackadar 1957; Parish and Oolman 2010; Du and Rotunno 2014), coastal boundary layer jets around the world (Ranjha et al. 2013) have also been studied extensively. These include the California coastal jet (e.g., Zemba and Friehe 1987; Burk and Thompson 1996; Pomeroy and Parish 2001), the Chilean coastal jet (e.g., Garreaud and Ricardo 2005; Jiang et al. 2010), the Somali jet (e.g., Krishnamurti et al. 1976; Chakraborty et al. 2009), the Carolina coastal jet (e.g., Sjostedt et al. 1990; Doyle and Warner 1993), the New York Bight jet (Colle and Novak 2010), and others. The coastal jets are frequently associated with large-scale atmospheric circulation, diurnal land–sea thermal contrast, and coastal terrain (Ranjha et al. 2013).

Baroclinicity and diurnal forcing near coasts play an important role in the development and diurnal variations

---

Corresponding author address: Dr. Yi-Leng Chen, Department of Atmospheric Sciences, SOEST, University of Hawai'i at Mānoa, 2525 Correa St., Honolulu, HI 96822.
E-mail: yileng@hawaii.edu

DOI: 10.1175/MWR-D-14-00348.1

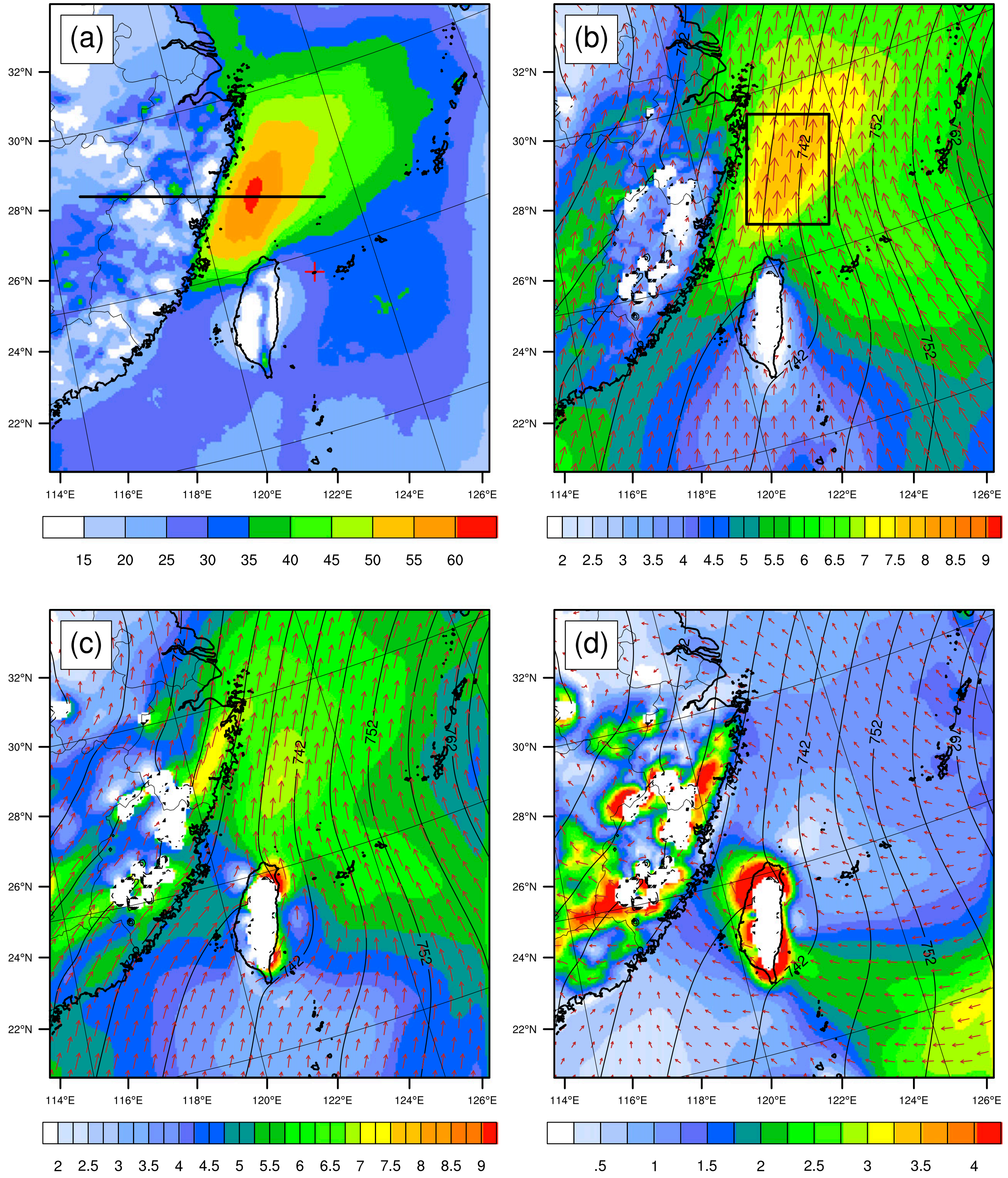

FIG. 1. Horizontal distributions of (a) the occurrence frequency (shaded, %) of BLJs [criteria for identifying BLJs is same as in Du et al. (2014)]; (b) average 925-hPa wind vectors, speed (shaded, m s^{-1}), and geopotential height (black solid lines, interval 5 gpm); (c) as in (b), but for geostrophic winds; and (d) as in (b), but for ageostrophic winds over southeastern China for July 2006–11 using the model data (REAL experiment). Black line in (a) is referenced in Figs. 2, 10, 14, and 19; and black box in (b) in Figs. 11 and 13.

TABLE 1. Configurations of the WRF Model used in this study.

Numerical and physical process	Schemes and model
Microphysics	WSM 6-class graupel
Longwave radiation	RRTM scheme
Shortwave radiation	Dudhia scheme
Surface layer	Monin–Obukhov
Land surface	Unified Noah
Planetary boundary layer	YSU
Cumulus parameterization	Kain–Fritsch

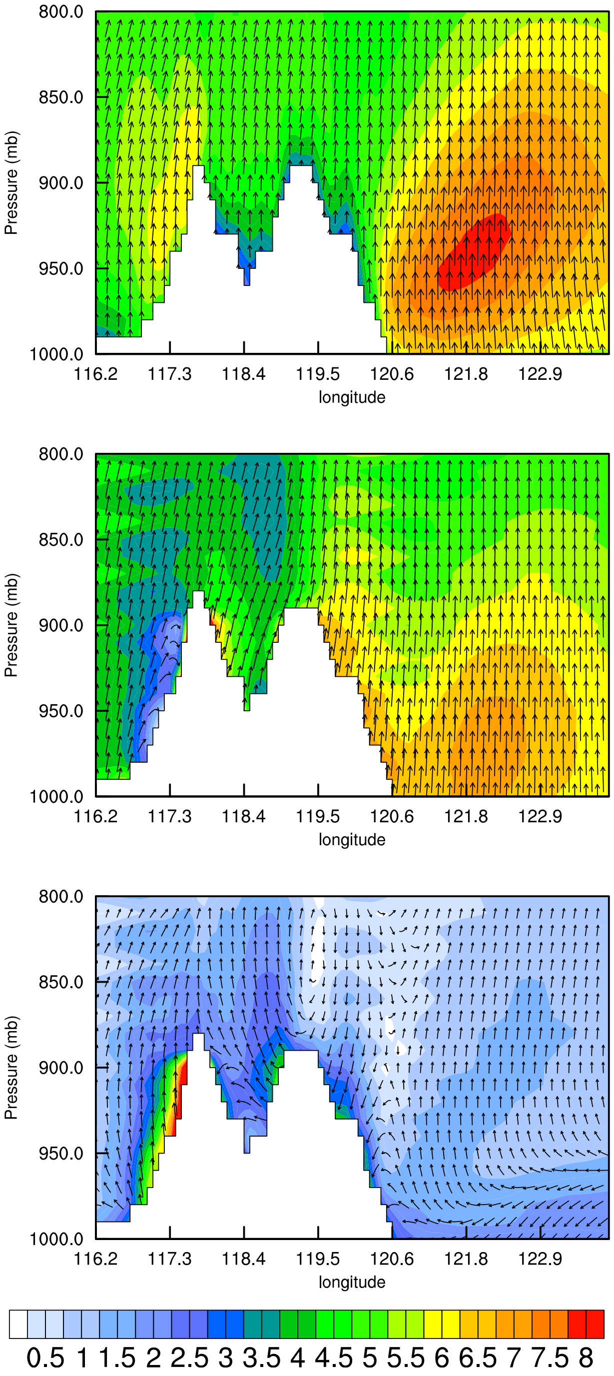

FIG. 2. Longitude–pressure cross sections of (a) the mean horizontal winds, (b) geostrophic winds, and (c) ageostrophic winds along the black line in Fig. 1a for July 2006–11. Color denotes wind speed (m s^{-1}). Wind vectors denote horizontal winds (e.g., upward means southerly winds).

of low-level winds and coastal jets. Small-scale land–sea breezes near the surface along the coast are well documented in several previous studies (Haurwitz 1947; Schmidt 1947; Rotunno 1983; Drobinski et al. 2011; Novak and Colle 2006). Using the linear theory of the sea breezes in an alongshore thermal wind, Drobinski et al. (2011) found that the daytime enhanced across-coast winds exhibit a clockwise rotation with an along-coast wind maximum at 1800 local time (LT). Zhang et al. (2006) studied the LLJs over the mid-Atlantic states and found that 90% of these jets exhibit a pronounced nocturnal maximum in the lowest 1.5 km with a jet core located near the middle portion of the sloping terrain. These jets are subgeostrophic during the daytime due to turbulence mixing in the lowest levels and become supergeostrophic after midnight consistent with the inertial oscillation mechanism proposed by Blackadar (1957). The southerly New York Bight jet offshore (east) of the northern New Jersey coast and south of Long Island occurs at ~150 m MSL within the sloping marine inversion with a diurnal maximum at 1900 eastern daylight time, which is approximately 1–2 h after the peak meridional pressure gradient, through a geostrophic adjustment process (Colle and Novak 2010). Along the California coast, the northerly jet is situated within a sloping marine inversion with the maximum coastal baroclinicity in the midafternoon (Burk and Thompson 1996). Burk and Thompson (1996) suggest that the delay of jet maximum in the early evening is associated with diurnal variations of baroclinicity (maximum in the midafternoon hours) along with inertial and friction effects. Furthermore, the northerly jets along the California coast are enhanced by a persistent synoptic-scale pressure gradient (North Pacific high

TABLE 2. A list of sensitivity experiments with different topography, surface fluxes, and smoothing procedures.

Expt	Description
REAL	Model dataset from Du et al. (2014) for July 2006–11 with smoothing between 1200 and 1100 UTC
NoTW	As in REAL, but with the Taiwan terrain completely removed and the land surface replaced with ocean
LowFJ	As in REAL, but with the Fujian terrain reduced to 10%
NoFlux	As in REAL, but with heat and moisture fluxes turned off at the surface without smoothing between 1200 and 1100 UTC

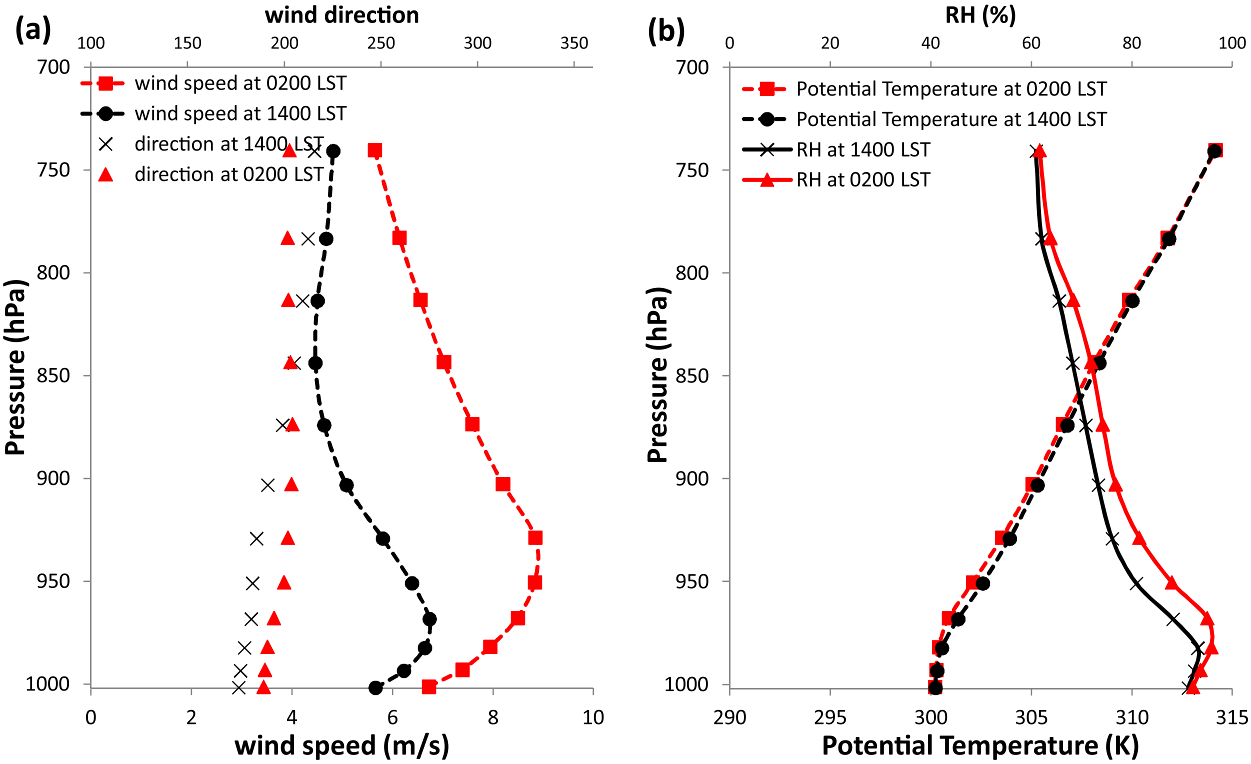

FIG. 3. Vertical profiles of (a) mean horizontal wind speed ($\mathrm{m\,s^{-1}}$) and direction (°), and (b) potential temperature (K) and relative humidity (%) at 1400 LST (black lines) and 0200 LST (red lines) from the model data at 28°N, 122°E (CBLJ core) for July averaged during 2006–11.

to the west, thermal low to the east) and the presence of coastal terrain.

In addition to baroclinicity and diurnal forcing, the orographic effect is another important factor in producing or enhancing coastal jets when a high mountain range exists along the coast. Examples of this include the Andes for the Chilean coastal BLJ (Jiang et al. 2010), the East African mountains for the Somali jet (Chakraborty et al. 2009), the Appalachians for the mid-Atlantic LLJs (Zhang et al. 2006), and the central mountain range for the Taiwanese barrier jets (Li and Chen 1998). Jiang et al. (2010) suggested that in addition to the baroclinic zone along the Chilean coast due to land–sea thermal contrast, the interaction between the Andes and the winds associated with the southeast Pacific high pressure system (SEPH) results in mesoscale high pressure off the southern Chilean coast that enhances the southerly Chilean coastal BLJ by increasing the equatorward pressure gradient force. These Chilean coastal boundary layer jets typically have a direction parallel to the coastline. Krishnamurti et al. (1976) demonstrated that the East African mountains provide a western boundary (barrier) that intensifies the Somali jet by deflecting westerly low-level air northward. Using sensitivity simulations, Zhang et al. (2006), showed that the intensity of the mid-Atlantic LLJ decreases from 12 to $9\,\mathrm{m\,s^{-1}}$ when the terrain of Appalachians is removed. A barrier jet that often occurs along the northwestern coast of Taiwan is a result of the deflected airflow along the western coast, which accelerates northward with a large cross-contour wind component down the orographically induced pressure gradients (Li and Chen 1998).

Using hourly model data with a 9-km resolution, Du et al. (2014) found that BLJs frequently occur off the southeastern coast of China in July [Fig. 1a; similar to Fig. 5f of Du et al. (2014)]. The criteria they employed to identify a BLJ is based on the existence of maximum wind speed of over $10\,\mathrm{m\,s^{-1}}$ below the 4-km height level with significant vertical shear. Figure 1a shows the frequent occurrences of BLJs off the southeastern coast of China with a maximum (about 60% frequency) around 28°N, 122°E from the model data for July 2006–11. Because few studies have documented the jet off the southeastern coast of China, several questions arise. 1) What are the characteristics of the coastal BLJ (CBLJ)? 2) Why does the CBLJ exist? 3) To what extent does the Taiwan and Fujian terrain affect the existence of the CBLJ? 4) Does the CBLJ have a diurnal variation? If so, what are the mechanisms for its diurnal variations? 5) What are the differences and similarities between the coastal jet off the southeastern China coast and other coastal jets

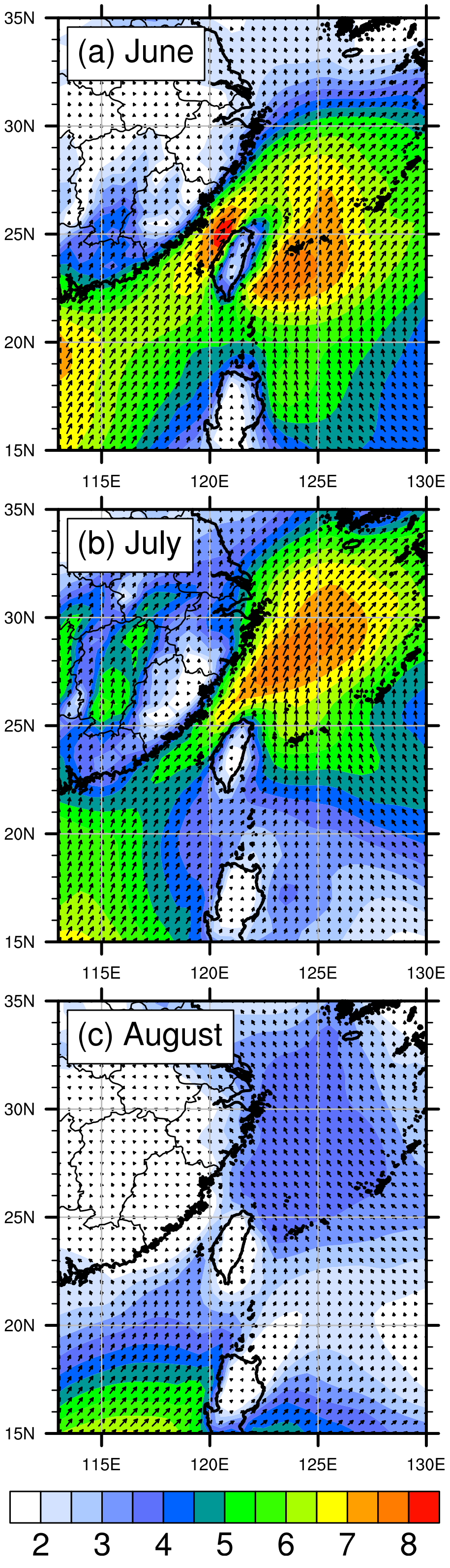

FIG. 4. Horizontal distributions of averaged 925-hPa wind vectors and speed (shaded, m s^{-1}) during (a) June, (b) July, and (c) August 2006–11 from the CFSR data.

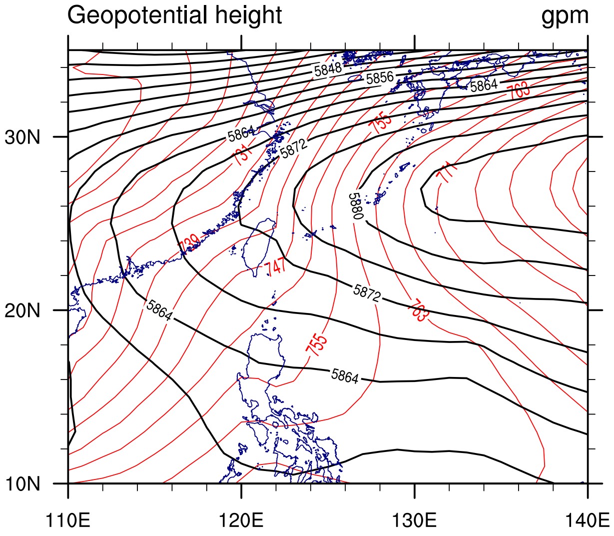

FIG. 5. The average 500-hPa (black contour) and 925-hPa (red contour) geopotential height for July 2006–11 from the NCEP FNL operational global analysis data on a 1° × 1° grid every 6 h.

found in the literature, including formation mechanisms and diurnal variations?

In this study, the model data during the period of July 2006–11 described by Du et al. (2014) are used to explore the mechanisms for the existence of the CBLJ and the reasons for its diurnal variations, if any. Detailed procedures for our numerical simulations are presented in section 2. In section 3, we describe the general climatological characteristics of the simulated CBLJ. The simulation result is compared to the high-resolution data from a wind profiler radar and the European Centre for Medium-Range Weather Forecasts (ECMWF's) operational model analysis with a 12-km resolution. In section 4, the mechanisms for diurnal variations of the CBLJ are diagnosed based on the model data. In section 5, the mechanisms discussed in section 4 are further explored with model sensitivity experiments (Table 2). The differences and similarities between this jet and other coastal jets found in the literatures are discussed in section 6. The final section summarizes our results.

2. Model and data

The Advanced Research Weather Research and Forecasting Model (WRF-ARW, version 3.3.1) with a 9-km horizontal resolution is used in this study. The model top was set at 50 hPa with 40 Eta layers[1] in the vertical. The

---

[1] The η-layer levels: 1.0000, 0.9974, 0.9940, 0.9905, 0.9850, 0.9800, 0.9700, 0.9600, 0.9450, 0.9300, 0.9100, 0.8900, 0.8650, 0.8400, 0.8100, 0.7800, 0.7500, 0.7100, 0.6800, 0.6450, 0.6100, 0.5700, 0.5300, 0.4900, 0.4500, 0.4100, 0.3700, 0.3300, 0.2900, 0.2500, 0.2100, 0.1750, 0.1450, 0.1150, 0.0900, 0.0650, 0.0450, 0.0250, 0.0100, and 0.0000.

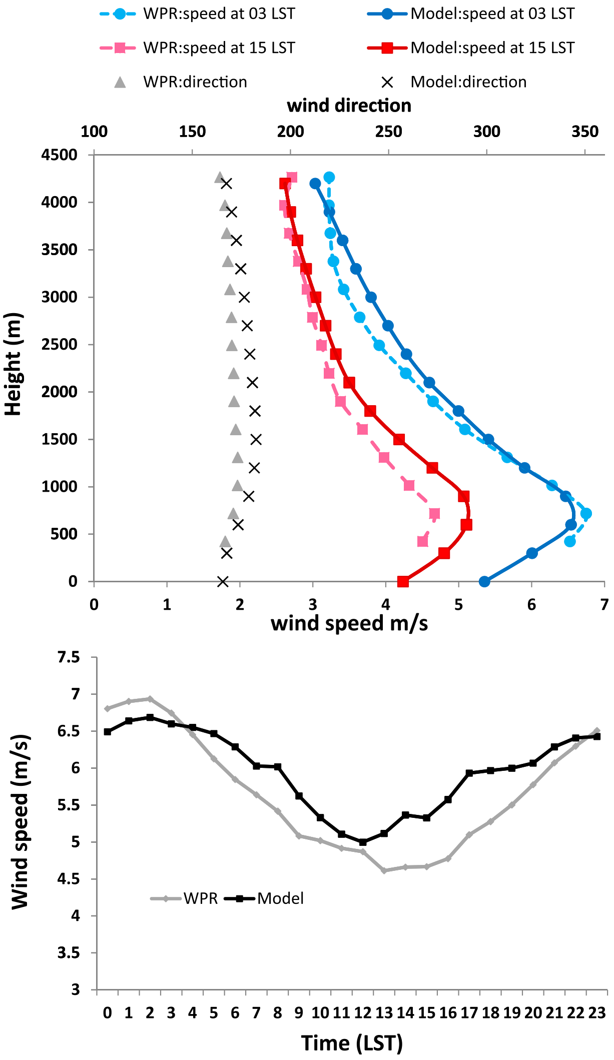

FIG. 6. (a) Mean vertical profiles of horizontal wind speed (m s^{-1}) and direction (°) for 0300 and 1500 LST from wind profiler radar (WPR) observations and the model data at Yonagunijima (24.47°N, 123.01°E) for July 2006–11. (b) Diurnal variations of wind speed at the 925-hPa level from wind profiler radar observations and the model data at Yonagunijima averaged over July 2006–11.

hourly outputs are generated from daily simulations over China during July from 2006 to 2011. The daily simulation, which is initialized by the National Centers for Environmental Prediction (NCEP) Final (FNL) Operational Global Analysis data (1° grid spacing), starts at 0000 UTC every day and runs for 36 h. Hourly model data from 1200 to 1100 UTC the following day are used to take into account the spinup issue. We implemented measures to eliminate the gap in the data between 1100 and 1200 UTC due to their different forecasting errors. For the commencing time of the daily output, we varied between 1200 and 0600 UTC with the corresponding ending time between 1100 and 0500 UTC the following day [Fig. 2 of Du et al. (2014)]. This reinitialization approach is widely adopted for regional climate simulations (Žagar et al. 2006; Jiménez et al. 2010; Parish and Oolman 2010; Zhang et al. 2012; Yang et al. 2005) and is an effective method to alleviate the problems of systematic model errors for a long-term integration (Lo et al. 2008). The model configurations are given in Table 1. A detailed description of the model configuration is given in Du et al. (2014).

To validate the model dataset for the CBLJ, the wind profiler radar (WPR) observation with high vertical resolution at Yonagunijima, Japan (24.47°N, 123.01°E, red cross in Fig. 1a), and the ECMWF atmospheric operational model analysis (starting in 2011) with 0.141° × 0.141° grids are used. The NCEP Climate Forecast System Reanalysis (CFSR; Saha et al. 2010) for June–August 2006–11 are used to study the seasonal variation of the CBLJ because it covers a longer period compared to the ECMWF data.

In addition to the model data (hereafter REAL experiment), three sensitivity experiments during the same period are performed (Table 2) to further study the mechanisms of the CBLJ. The NoFlux experiment is conducted to investigate the impacts of surface fluxes on the mean state and the diurnal variations of the CBLJ. The NoTW and LowFJ experiments are performed to explore the effects of Taiwan and Fujian terrain on the CBLJ.

3. Climatological characteristics of the simulated CBLJ and validation

Figure 1b shows the horizontal distribution of the simulated mean winds at the 925-hPa level during July with a maximum wind speed of ~8 m s^{-1} around 28°N, 122°E off the southeastern coast of China. The simulated mean wind direction associated with the wind speed maximum is nearly parallel to the coastline (southerly, Fig. 1b). The simulated jet exhibits a maximum in the vertical wind profile at the 925-hPa level (Fig. 2a), which is above the mixed layer (Fig. 3).

The horizontal distributions of mean winds at the 925-hPa level during June, July, and August from CFSR (Fig. 4) show that the CBLJ off the southeastern coast of China exhibits pronounced seasonal variations with a maximum in July. In June, the CBLJ occurs east of Taiwan and a barrier jet occurs along the northeastern coast of Taiwan (Li and Chen 1998). In August, the CBLJ becomes weak as the west Pacific subtropical high (WPSH) moves northward.

In July, the WPSH is located east of China with the ridge axis around 26°N at the 500-hPa level (Fig. 5). The CBLJ occurs west of the WPSH with large synoptic

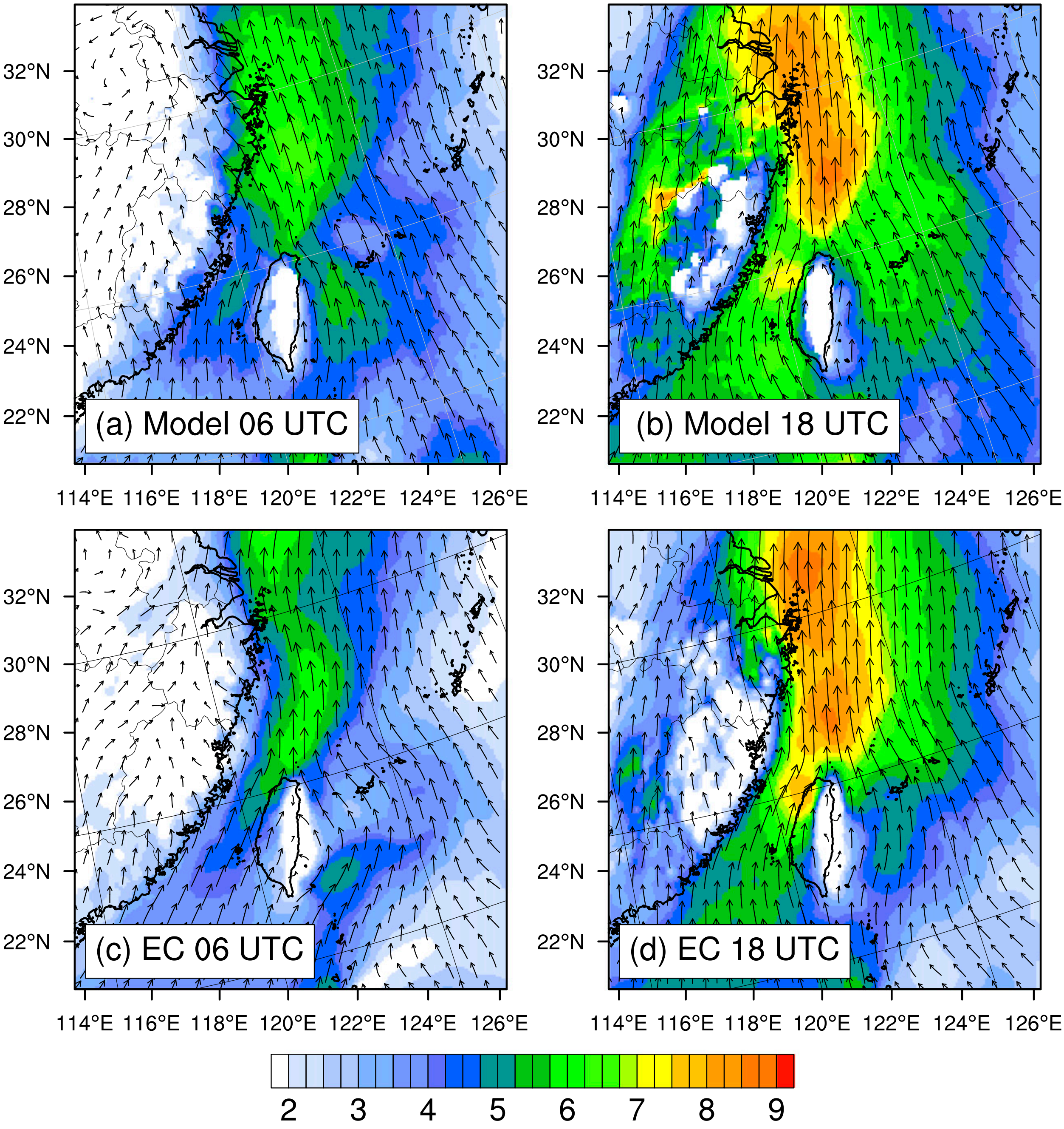

FIG. 7. The averaged 925-hPa wind vectors and speed (shaded, m s^{-1}) for (left) 0600 UTC (1400 LST) and (right) 1800 UTC (0200 LST) July 2011 from (a),(b) the model and (c),(d) the ECMWF's operational model analysis.

pressure gradients at low levels (Fig. 5). The land–sea thermal contrast may enhance the low-level geopotential height gradients along the eastern coast of China (Fig. 5). Near the core (~925 hPa) of the CBLJ, the geostrophic winds (about 7 m s^{-1}) account for about 87% of the total winds (about 8 m s^{-1}) (Fig. 1c). Geostrophic winds are larger at low levels and largest at the surface (Fig. 2b). However, the wind speed maximum of the vertical wind profile of the CBLJ is located at about the 925-hPa level because of friction and vertical mixing near the surface (Fig. 2c). It appears that the CBLJ represents an enhancement of the background synoptic flow on the southeastern flank of the WPSH by the land–sea thermal contrast and orographic effects of the coastal terrain where the coastline is almost parallel to the isobars (Fig. 1). It is possible that the terrain of Taiwan also

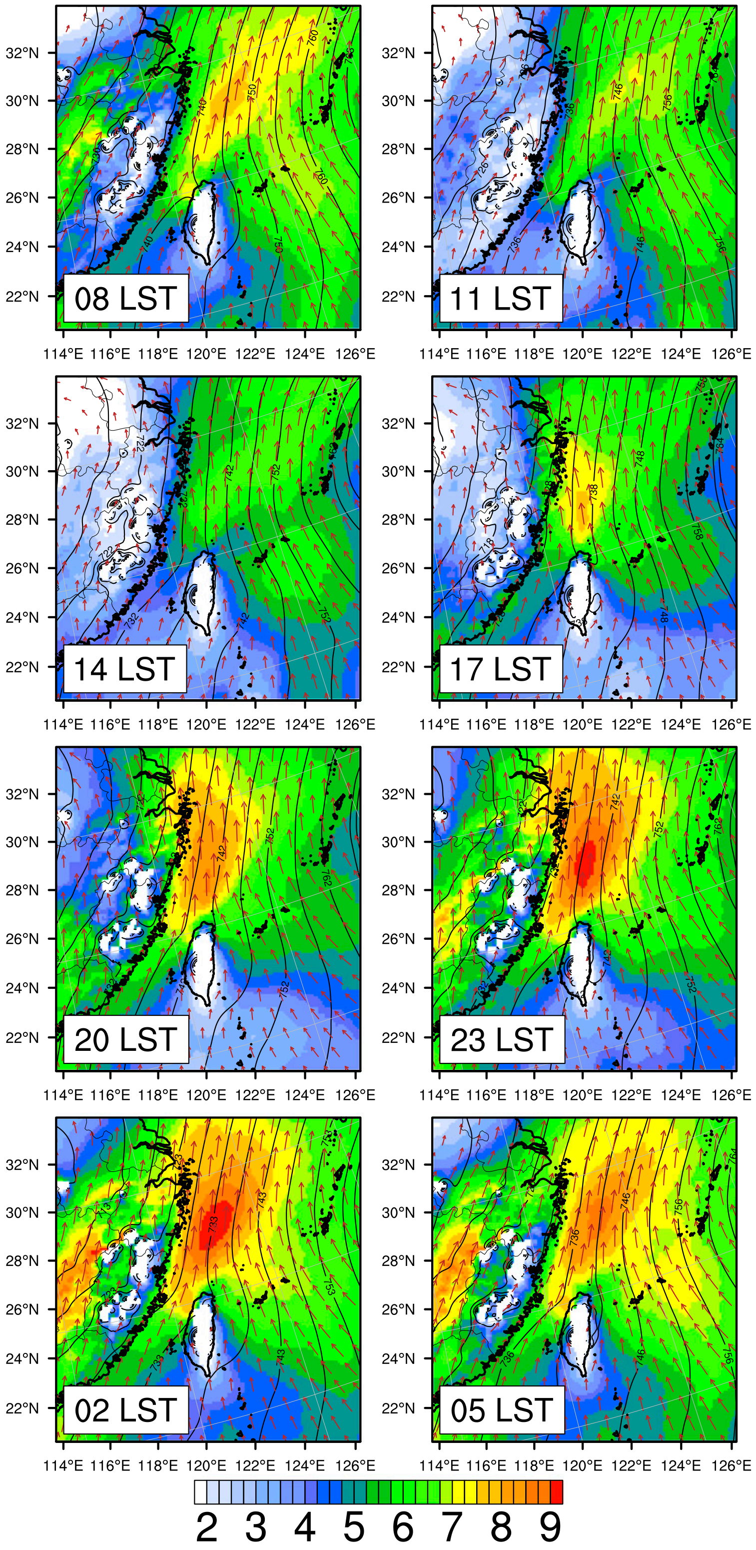

FIG. 8. Diurnal variations (0800, 1100, 1400, 1700, 2000, 2300, 0300, and 0500 LST) of the 925-hPa wind vectors and speed (shaded, m s^{-1}) and geopotential height (black contours, interval 5 gpm) for July 2006–11 from the model data (REAL experiment).

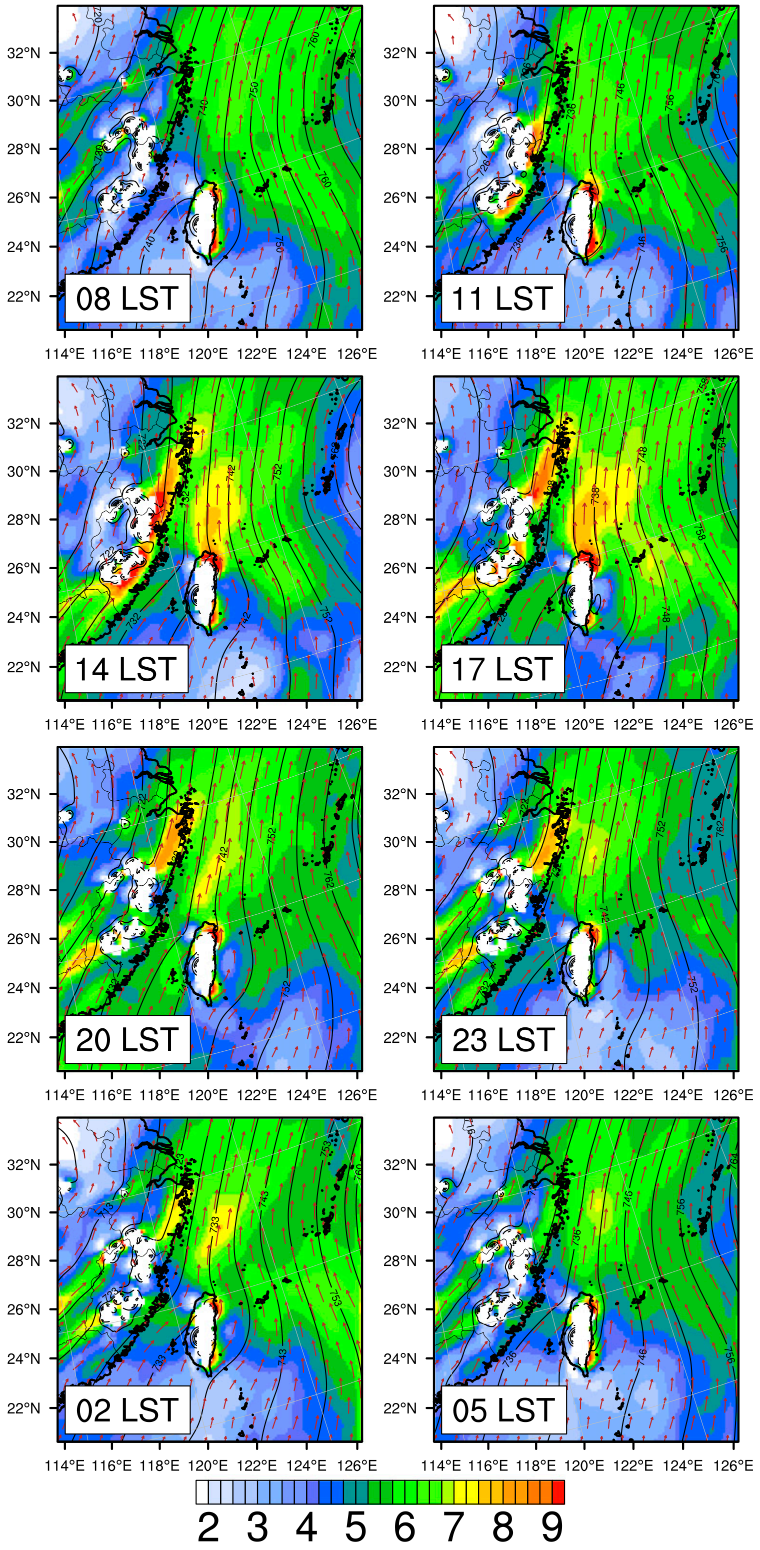

FIG. 9. As in Fig. 8, but for geostrophic winds (shaded, m s^{-1}).

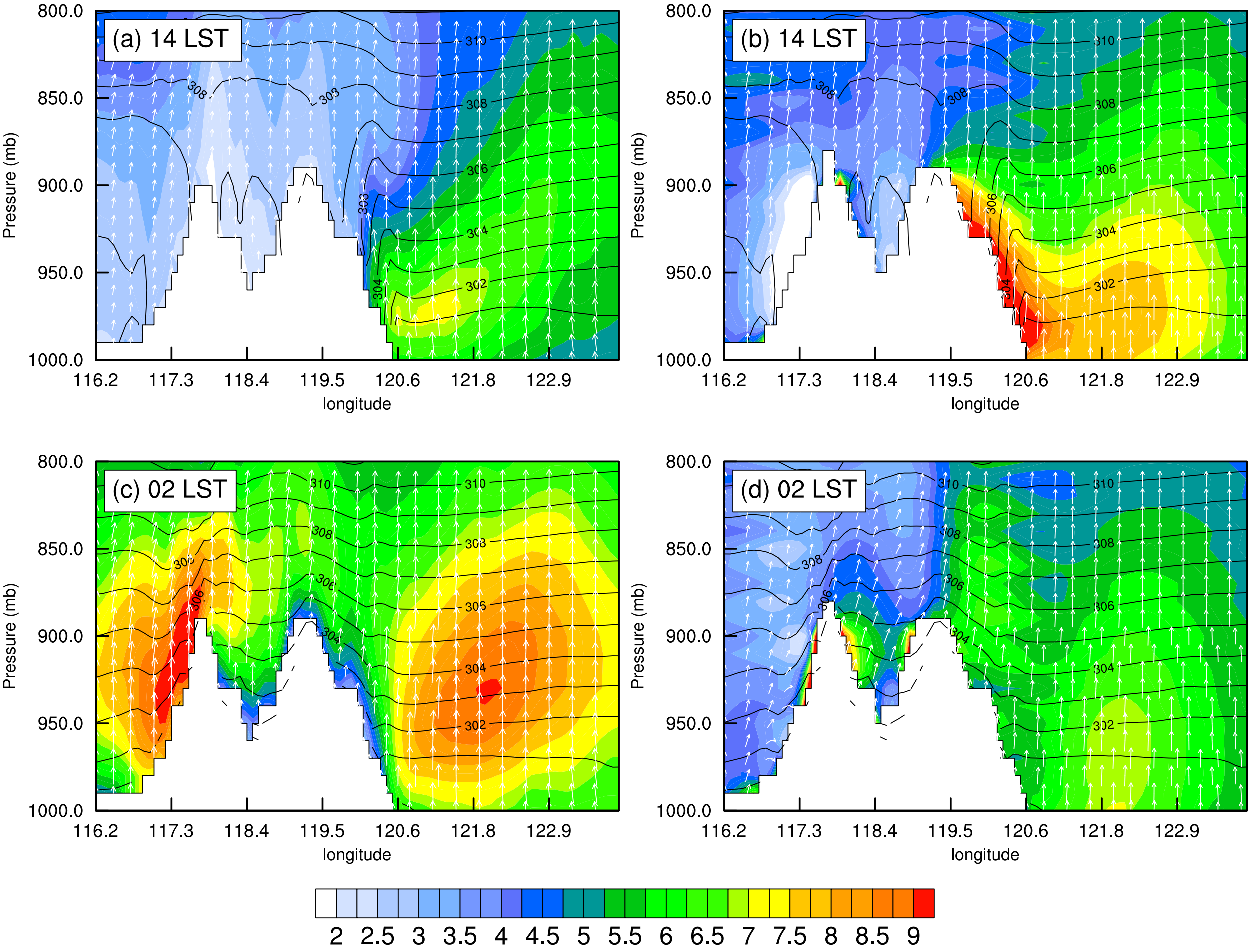

FIG. 10. Longitude–pressure cross sections of potential temperature (contours, K) and (a),(c) the mean horizontal winds and (b),(d) geostrophic winds at (top) 1400 and (bottom) 0200 LST along the black line in Fig. 1a for July 2006–11. Color denotes wind speed. Wind vectors denote horizontal winds (e.g., upward means southerly winds).

affects the CBLJ. This possibility will be studied using model sensitivity tests and discussed in section 5.

Du et al. (2014) used sounding and wind profiler radar observations at a few locations over China to evaluate the model data. To further verify the simulated CBLJ and its diurnal variations, the WPR data at Yonagunijima near the CBLJ and the ECMWF atmospheric operational model analysis are also used for model verifications. The mean vertical wind profiles at 0300 LST (1900 UTC)[2] and 1500 LST (0700 UTC) (Fig. 6a) from the model output are validated with the high vertical-resolution WPR data at Yonagunijima. The observed vertical wind profiles with a maximum at the 600-m level are simulated. The observed daytime versus nighttime differences in wind speeds at the 925-hPa level with a maximum around 0200 LST are also reproduced in the model (Fig. 6b), although the simulated wind speed minimum occurs 1–2 h earlier (1200 LST versus 1400 LST) and the simulated wind speed diurnal cycle amplitude is smaller ($<1\,\mathrm{m\,s^{-1}}$) as compared to the observations. The horizontal distributions (maximum wind speed around 0200 LST at 28°N, 122°E off the southeastern coast of China) of the CBLJ and its temporal variations with a nocturnal maximum from the model data are consistent with the ECMWF operational model data in July 2011 (Fig. 7). The wind speeds from the ECMWF operational model data are slightly stronger ($<1\,\mathrm{m\,s^{-1}}$) than that of our model data south of Taiwan and over the southern China plain.

4. Diagnosis of the diurnal variations of the simulated CBLJ

The simulated CBLJ strength exhibits pronounced diurnal variations with a nocturnal maximum ($\sim 9\,\mathrm{m\,s^{-1}}$)

---

[2] Local standard time (LST) is 8 h ahead of the coordinated universal time (UTC).

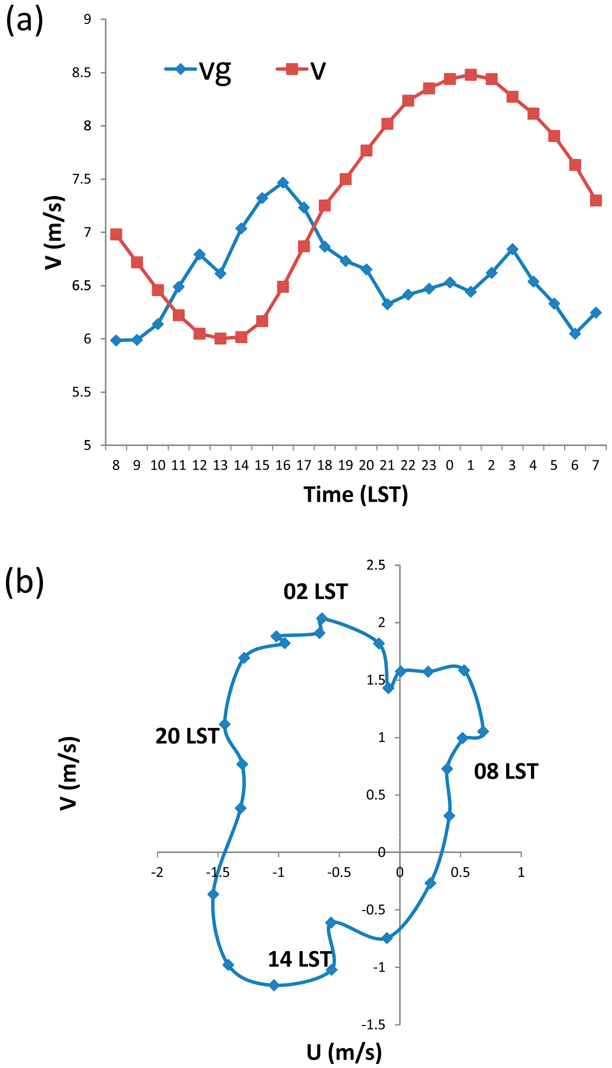

FIG. 11. (a) Diurnal variations of the mean 925-hPa wind component (v) and geostrophic wind (v_g) component for the y direction averaged over the coastal area (black box in Fig. 1b) in the REAL experiment. (b) A clockwise rotation of the mean 925-hPa ageostrophic wind averaged over the coastal area (black box in Fig. 1b).

around 0200 LST (Fig. 8). However, the geostrophic winds at the 925-hPa level show diurnal variations with a maximum ($>7\,\mathrm{m\,s^{-1}}$) in the late afternoon (1700 LST) (Fig. 9). Figure 10 shows longitude-pressure cross sections of the mean horizontal winds and geostrophic winds at 1400 and 0200 LST along the black line in Fig. 1a. Geostrophic winds are stronger near the coast (the slope of mountains) in the afternoon than at night (Figs. 10b and 10d) due to stronger thermal contrast in the afternoon near the coast. However, mean horizontal winds are stronger at night than in the afternoon and the location of the maximum wind speed is different from that of the geostrophic winds (Figs. 10a and 10c). The diurnal variations of the 925-hPa v-wind component and the v component of the geostrophic wind (v and v_g) averaged over the coastal area (denoted by a black box in Fig. 1b) for July 2006–2011 (Fig. 11a) are different. The v-wind component averaged over the black box has a maximum ($\sim 8.5\,\mathrm{m\,s^{-1}}$) at 0200 LST, whereas v_g exhibits a diurnal maximum ($\sim 7.5\,\mathrm{m\,s^{-1}}$) at 1600 LST. A clockwise rotation of the ageostrophic winds at the 925-hPa level off the coast is apparent (Fig. 11b) with easterly ageostrophic winds at 1700 LST, which become southerly ageostrophic winds ($\sim 2\,\mathrm{m\,s^{-1}}$) at 0200 LST (Fig. 12). The southerly ageostrophic winds at night plus southerly large-scale geostrophic winds result in maximum wind speed at night. Therefore, the diurnal variations of v are mainly attributed to the veering of ageostrophic winds. The rotation of winds is also documented in other observational studies (Song et al. 2005; Du et al. 2012).

To further investigate the mechanism for the diurnal variations of the CBLJ, the momentum balance is analyzed using the same method as Du et al. (2014). The y-component momentum equation can be written as

$$\frac{\partial v}{\partial t} = \left(-u\frac{\partial v}{\partial x} - v\frac{\partial v}{\partial y}\right) - \frac{\partial \Phi}{\partial y} - fu + F$$

or

$$\underset{\text{I}}{\frac{\partial v}{\partial t}} = \underset{\text{II}}{\left(-u\frac{\partial v}{\partial x} - v\frac{\partial v}{\partial y}\right)} \underset{\text{III}}{-f(u-u_g)} + \underset{\text{IV}}{F}$$

The above equation states that the local acceleration of the v-component wind (term I) equals the sum of the horizontal advection (term II), the Coriolis force acting on the ageostrophic winds in the y direction (term III), and friction (residual term, term IV). Figure 13 shows the diurnal variations of the four terms in the momentum equation at the 925-hPa level averaged over the coastal area (Fig. 1b, black box). It is apparent that the Coriolis force acting on the ageostrophic winds (term III) is the dominant term when compared to the horizontal advection (term II) and friction (term IV). Unlike over land [e.g., Tarim basin, northeastern China, and southeastern China; Du et al. (2014)], the friction term plays a relatively minor role in the deceleration of v in the daytime due to relatively weak vertical turbulence mixing in the marine boundary layer (Fig. 13).

The inertial oscillation mechanism proposed by Blackadar (1957) was triggered by the sudden suppression of turbulence in the mixed layer at sunset. During the daytime, the wind in the mixed layer is subgeostrophic

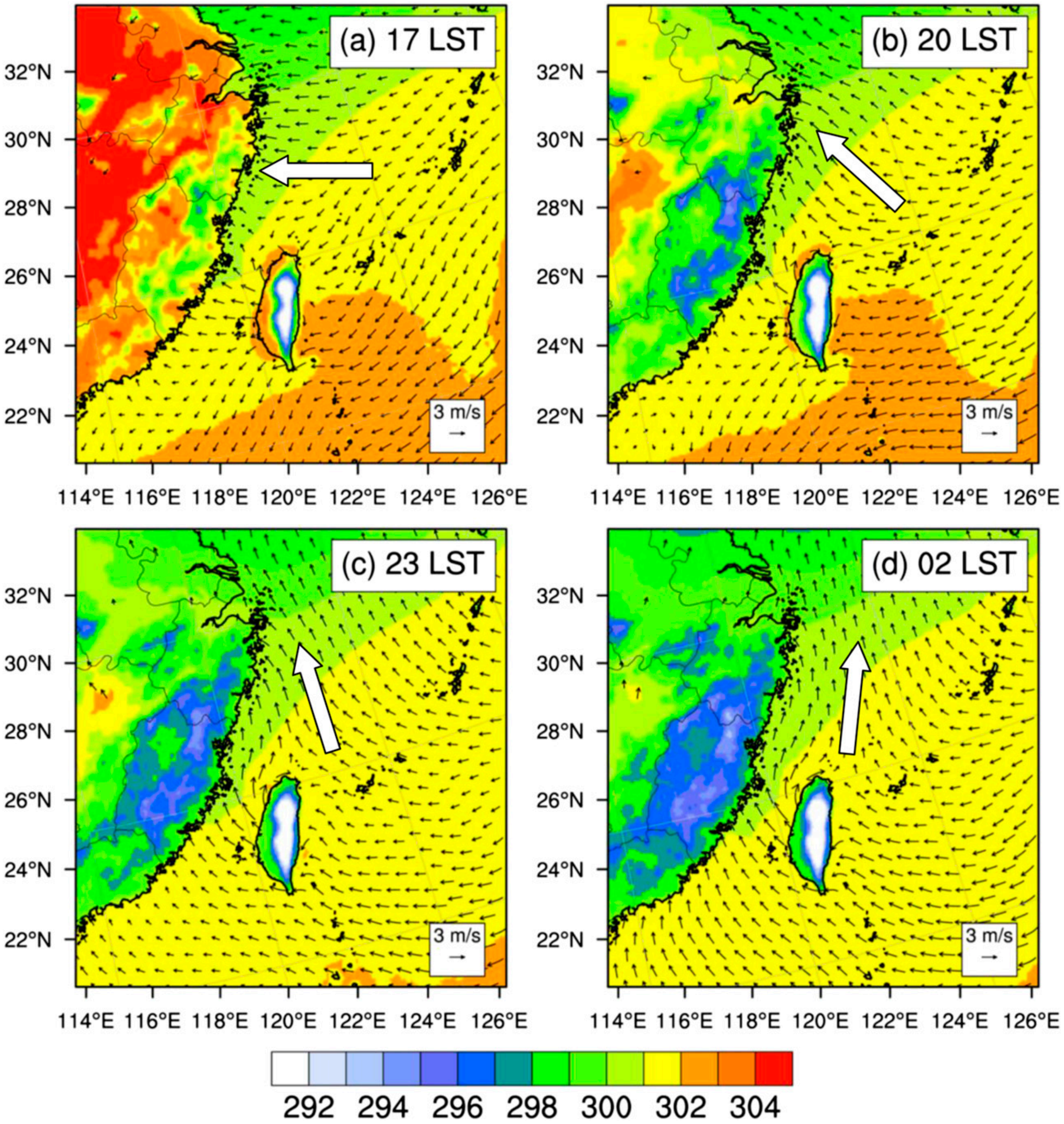

FIG. 12. The averaged 925-hPa ageostrophic wind vectors and surface temperature at 2 m (shaded, K) for 1700, 2000, 2300, and 0200 LST in the REAL experiment July 2006–11. White arrows denote the main directions of the perturbation wind vector over the CBLJ region.

due to strong vertical turbulence mixing. After sunset, a stable layer develops near the surface as a result of nocturnal cooling, and the air just above the stable layer becomes frictionless. The ageostrophic wind veers under the Coriolis force and undergoes an inertial oscillation that leads to supergeostrophic flow during a portion of the oscillation several hours later (Blackadar 1957; Zhang et al. 2006). In contrast to the air above the land surface (e.g., Du et al. 2014), the friction term for the air above the ocean surface is rather small for the entire day (Fig. 13). Where do the ageostrophic winds off the coast come from? Because of the presence of east–west thermal contrast, at 1400 LST a thermal circulation with upward vertical motions over land and downward vertical motion over the ocean forms near the coast and leads to easterly ageostrophic winds at low levels off the

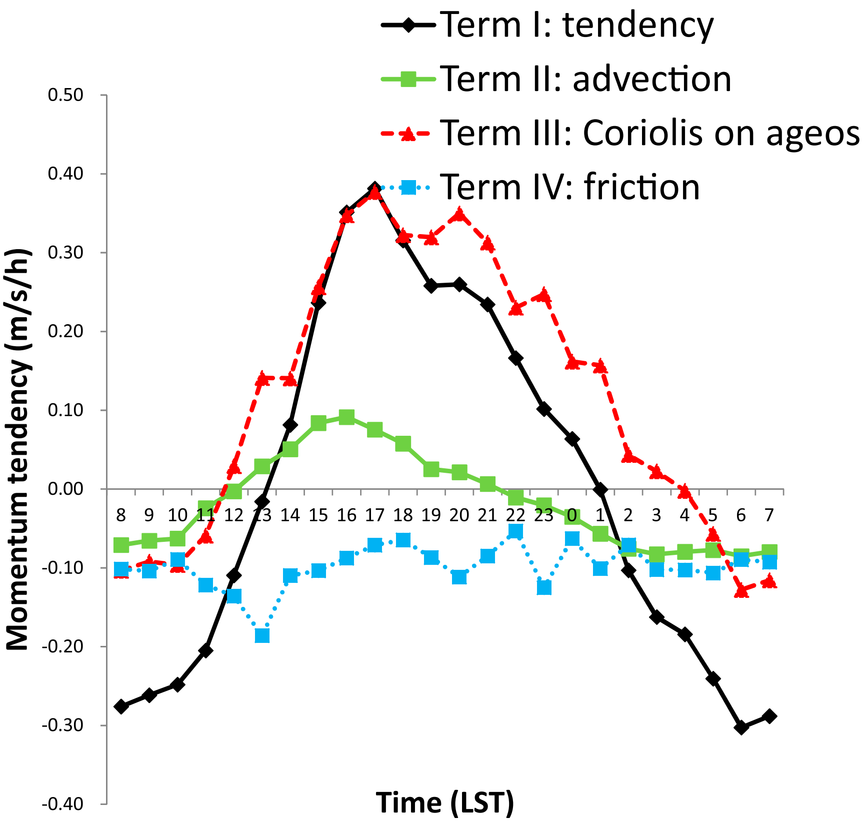

FIG. 13. Diurnal variations of individual terms in the horizontal momentum equation at the 925-hPa level averaged over the coastal area (black box in Fig. 1b) for July 2006–11 in the REAL experiment.

coast (Fig. 14a). However, the thermal circulation in the evening is not significant at the 925-hPa level, which is above the surface layer (Fig. 14c). The effect of the Coriolis force on the easterly ageostrophic winds over the ocean, which is caused by the land–sea thermal contrast in the late afternoon hours, is the dominant term (Fig. 13) for the development of supergeostrophic winds at night. It appears that the nocturnal CBLJ maximum is related to inertial oscillation initiated by the disappearance of land surface heating after sunset. The impact of land–sea thermal contrast on CBLJ will be discussed further in section 5a by removing surface fluxes in the model. Additional tests on the orographic effects, if any, of the coastal mountain ranges along the southeastern coast of China and Taiwan terrain on the strength and diurnal variations of the CBLJ will be discussed in section 5b.

5. Model sensitivity tests

a. Without surface fluxes

Because the land–sea thermal contrast is mainly caused by surface fluxes, a sensitivity experiment (NoFlux) during the same period without surface heat and moisture fluxes in the model is performed (Table 2) to investigate the impact of land–sea thermal contrast on the mean state and the diurnal variations of the CBLJ.

Without surface fluxes, the mean thermal contrast between land and ocean becomes rather small, which is from large-scale initial conditions, and the geopotential height gradients along the eastern coast of China are smaller than the REAL run (Figs. 1b and 15). Without surface fluxes, the subtropical high is also weaker. The maximum wind speed (about 6 $\mathrm{m\,s^{-1}}$) associated with the CBLJ at the 925-hPa level for the NoFlux experiment is about 2 $\mathrm{m\,s^{-1}}$ slower than the REAL experiment (Figs. 1b and 15). It is apparent that without differential heating between the China plain and the western Pacific in July, the CBLJ is weaker. The importance of the large-scale geostrophic balance associated with the WPSH and the thermal forcing (baroclinic zone) along the coast for the CBLJ is similar to that found along the California (Burk and Thompson 1996) and Chilean coasts (Jiang et al. 2010).

The NoFlux experiment is also used to diagnose the diurnal variations of the CBLJ. In the NoFlux

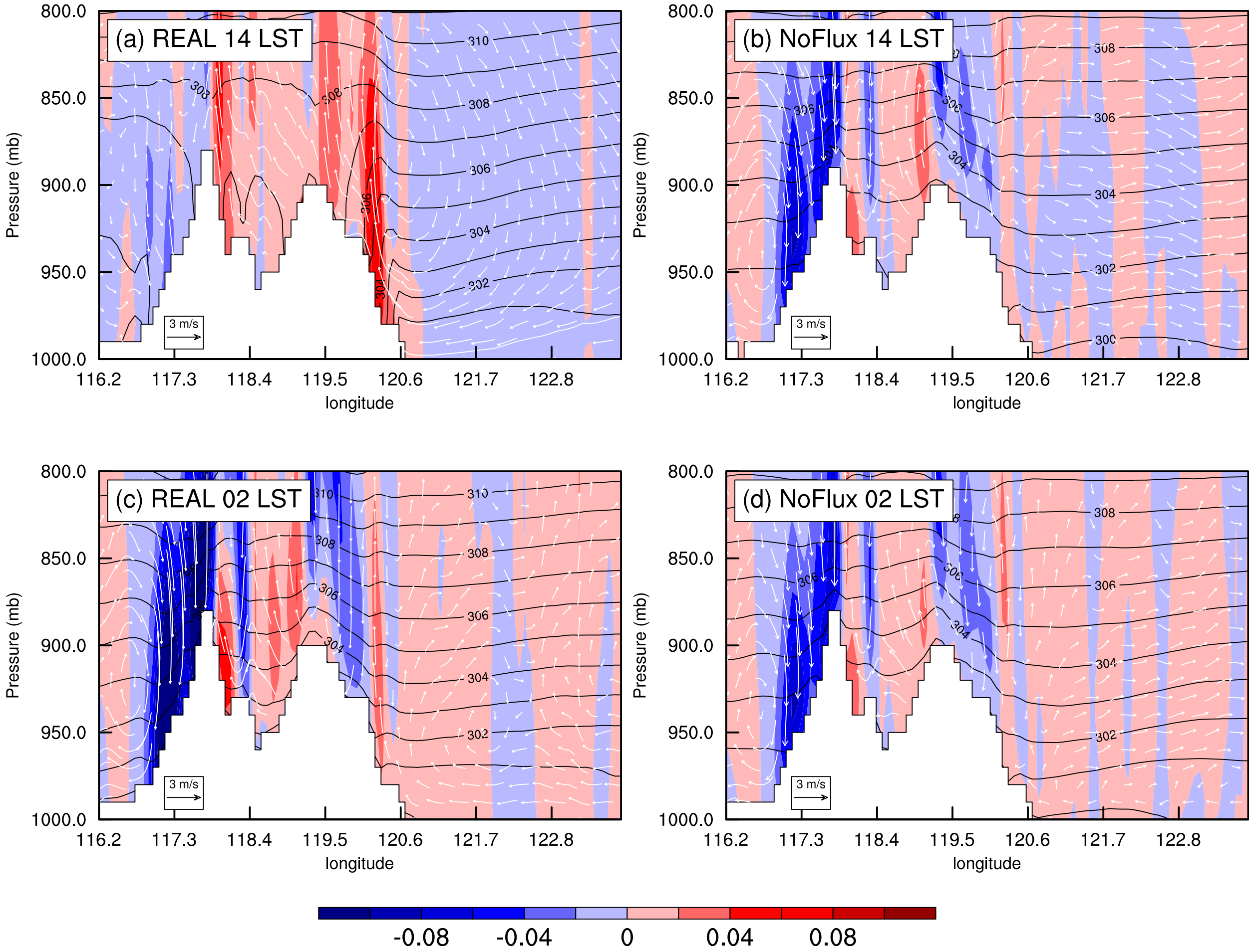

FIG. 14. Longitude–pressure cross section of vertical motion (shaded, cm s^{-1}), potential temperature (contours, K), and vertical circulation vectors (ageostrophic zonal wind and 100 times the vertical velocity) along the black line in Fig. 1a at (a),(b)1400 and (c),(d) 0200 LST for July 2006–11 for (a),(c) the REAL and (b),(d) NoFlux experiments.

experiment, the ageostrophic winds off the coast are much weaker than in the REAL experiment (Fig. 16) due to the absence of diurnal land–sea thermal contrast and thermally driven circulation near the coast (Figs. 14b and 14d). The weak ageostrophic winds off the northwestern Taiwan coast (barrier jet along northwestern Taiwan) are related to island blocking. The clockwise rotation of the ageostrophic winds off the southeastern China coast simulated in the NoFlux experiment is also not significant. Without fluxes at the surface, both the v-component wind (v) and the geostrophic wind component for the y direction (v_g) at the 925-hPa level decrease from 1200 UTC (2000 LST) (commencing time in the model) to 1100 UTC (1900 LST) the following day (Fig. 17a) due to a decreasing thermal difference between land and sea in the NoFlux experiment (Fig. 16). In contrast to the REAL experiment, all four terms in the momentum equation exhibit little diurnal variation in the NoFlux experiment (Fig. 17b). The most striking difference between the REAL and NoFlux experiments is the difference in the Coriolis force acting on the ageostrophic wind term (term III). This term has small negative values throughout the entire diurnal cycle in the NoFlux experiment (Fig. 17b), but it has large positive values during the day with decreasing magnitude until the early morning in the REAL experiment (Fig. 13b). Thus, diurnal variations of the CBLJ in the NoFlux experiment are not significant due to weaker ageostrophic winds off the coast of southeastern China. It is apparent that thermally driven circulations, caused by land–sea thermal contrast, impact the ageostrophic winds off the coast and the Coriolis force acting on it.

b. *Orographic effects*

In this section we explore the effects of Taiwan and Fujian terrain on the CBLJ using two model sensitivity experiments: 1) NoTW where the Taiwan terrain is

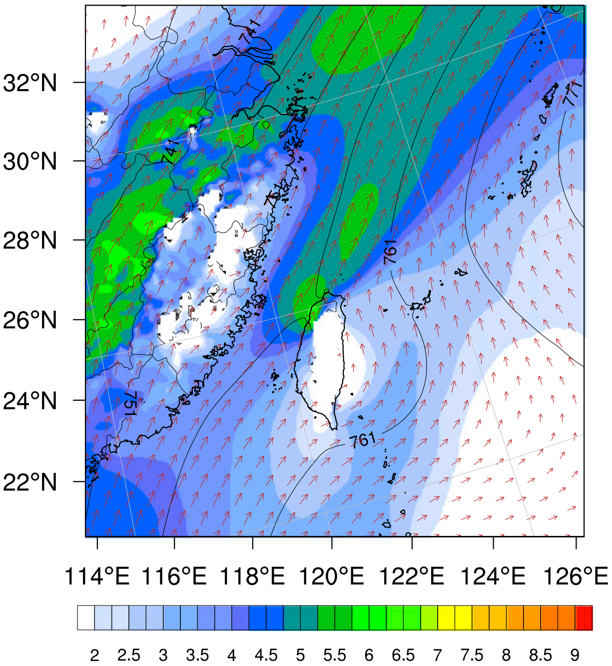

FIG. 15. As in Fig. 1b, but for the NoFlux experiment.

removed completely and the land is replaced with ocean, and 2) LowFJ where the Fujian terrain is reduced to 10% of the actual terrain height (Table 2).

Figure 18a shows the difference in wind vectors at the 925-hPa level between the REAL experiment and the NoTW experiment. The Taiwan terrain does indeed affect the magnitude of the CBLJ (around 0.6 m s^{-1}) as a result of orographic blocking. From the difference of geopotential height between REAL and NoTW experiments (Fig. 18a), we find that the low-level incoming southwesterly flow decelerates off the southwestern coast of Taiwan when it encounters the orographically induced high pressure there (geopotential height difference ~0.8 gpm). The flow accelerates along the northwestern coast of Taiwan due to the orographically induced pressure gradients. This orographic blocking is more pronounced at night (geopotential height difference ~1.2 gpm, Fig. 18e) than in the afternoon (geopotential height difference ~0.6 gpm, Fig. 18c) due to changes in stability over land. Lin et al. (2011) also found that the barrier jet along the northwestern Taiwan coast is stronger in the early morning than in the afternoon. When the terrain of Taiwan is included, the pressure in the exit region is lower with stronger winds (0.5–1 m s^{-1}) north of the Taiwan Strait (Fig. 18a), especially at night (Figs. 18e and 19a,c).

The differences in winds and geopotential height between the REAL and LowFJ experiments are shown in Fig. 18b. The Fujian terrain also decelerates the incoming southwesterly flow with orographically induced higher pressure upstream (geopotential height difference ~1.2 gpm). The Fujian terrain also results in lower pressure or a cyclonic lee vortex downstream of the terrain along the southeastern China coast, which makes the winds north of the exit region of the Taiwan Strait stronger (0.5–1 m s^{-1}, Fig. 18b). At night (Fig. 18f), the leeside vortex is stronger due to more significant orographic blocking than in the afternoon (Fig. 18d). With orographic effects, the wind speed of the CBLJs located at the channel exit region is slightly stronger at night (Figs. 18f and 19b,d).

It is apparent that orographic blocking by the island terrain of Taiwan and the mountain range along the southeastern China coast contribute to a stronger CBLJ in the channel exit, especially at night. The diurnal variations of the blocking effect also partly contribute to the simulated nocturnal maximum in the CBLJ.

6. Discussion

In this study, we compare the CBLJ of China with two U.S. East Coast jets: 1) the New York Bight coastal jet (Colle and Novak, 2010) and 2) the low-level jet over the mid-Atlantic states (Zhang et al. 2006). These two jets have similar large-scale settings as compared to the CBLJ of China, which is located along the west-northwest periphery of the subtropical high. Both studies stressed the importance of the large-scale geostrophic forcing, land–sea thermal contrast, and terrain for the development of these coastal jets. However, differences exist among these jets, especially the time phases of diurnal variations and their mechanisms. These differences could be attributed to differences in the adjacent terrain and the geometry of the coastlines.

Colle and Novak (2010) studied the southerly New York Bight coastal jet, which is a part of large-scale enhancement by land–sea thermal difference. The maximum jet winds at 1900 LST are mainly due to the large meridional pressure gradient (north–south land–sea thermal contrast) at 1730 LST and subsequent geostrophic adjustment process. In contrast to the New York Bight jet, where both west–east and south–north thermal contrast exist, the CBLJ of China is located offshore of the east coast of the China plain where the land–sea thermal contrast is mainly in the east–west direction. In the afternoon, the east–west pressure gradient results in easterly ageostrophic winds toward the coast. The ageostrophic flow turns clockwise due to an inertial oscillation of the Coriolis force and becomes a southerly ageostrophic flow around 0200 LST when the southerly CBLJ becomes supergeostrophic and reaches a nocturnal maximum. Orographic blocking by the terrain of Taiwan and Fujian is more significant at night with a stronger southerly wind

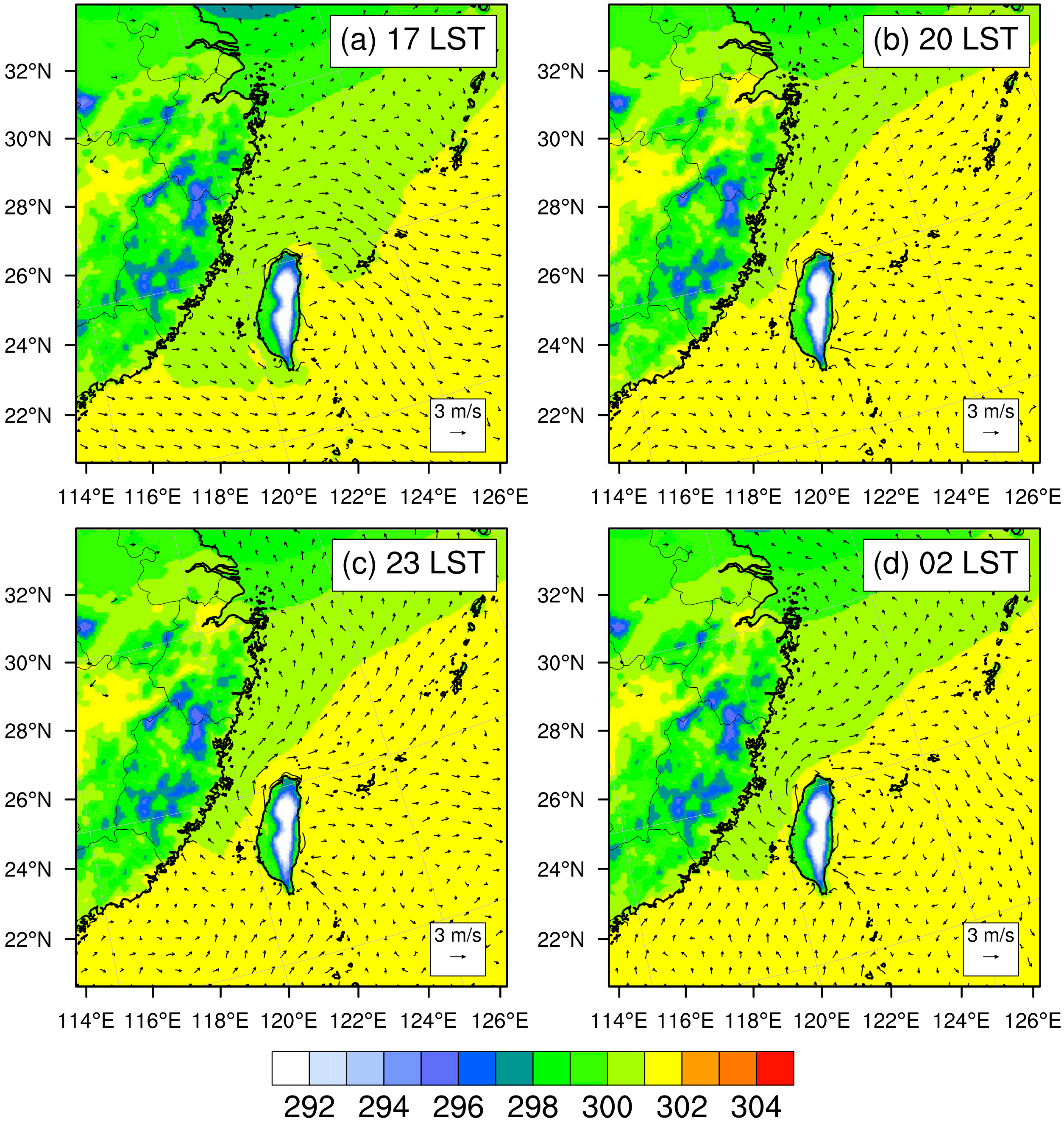

FIG. 16. As in Fig. 12, but for the NoFlux experiment.

component north of the Taiwan Strait than in the afternoon hours, which also contributes to the nocturnal maximum for the CBLJ of China.

Although both the CBLJ of China and the LLJ over the mid-Atlantic states have a nocturnal maximum, the physical processes are different. From their sensitivity simulations, Zhang et al. (2006) found that diurnal surface heat fluxes (over land) are responsible for the diurnal variations of the LLJ through inertial oscillation of ageostrophic winds triggered by a sudden suppression of turbulence by the development of a stable nocturnal boundary after sunset (Blackadar 1957). Over the mid-Atlantic states, the BLJ occurs above a sloping mountain terrain. The CBLJ of China, however, is above the marine mixed layer over the ocean where the eddy viscosity and vertical mixing are relatively small and do not have

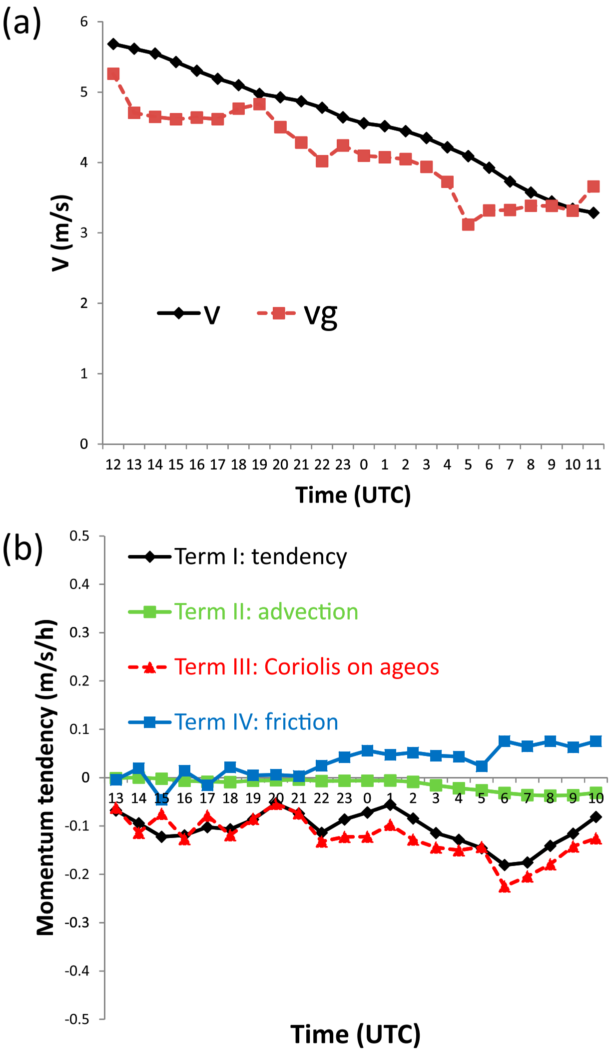

FIG. 17. (a) As in Fig. 11a, but for the NoFlux experiment. (b) As in Fig. 13, but for the NoFlux experiment.

significant diurnal variations. The ageostrophic wind off the coast in the afternoon hours is caused by land–sea thermal contrast rather than turbulence mixing in the daytime mixed layer. The nocturnal maximum for the CBLJ of China is mainly attributed to the veering of ageostrophic winds offshore due to the disappearance of land surface heating over the China plain after sunset.

7. Summary

Coastal boundary layer jets (CBLJs) have been studied extensively throughout different parts of the world. Because of the limitations of observational data, the CBLJ off the southeastern coast of China has not been previously documented. In this study, a long-term simulation using a high-resolution Nonhydrostatic Mesoscale Model (e.g., WRF) with reinitialization, which is achieved by subdividing a long-term continuous integration into shorter ones (36 h), is used to produce a 6-yr July dataset (2006–11) with a grid spacing of 9 km and 40 vertical levels in China (Du et al. 2014). This dataset is validated with ECMWF operational model analysis and high vertical resolution data from the radar wind profiler observations collected at Yonagunijima, Japan (24.47°N, 123.01°E). From the analysis of this dataset, we discover a pronounced CBLJ off the southeastern coast of China (around 28°N, 122°E) with a jet core (~8 $\mathrm{m\,s^{-1}}$) at the 925-hPa level. The CBLJ exhibits appreciable diurnal variations with a maximum of ~9 $\mathrm{m\,s^{-1}}$ at night (0200 LST).

Large-scale settings enhanced by land–sea thermal forcing are the main factors for the existence of the CBLJ. The axis of the CBLJ is located west of the WPSH and near the coast where the geopotential height gradients are the largest. The geostrophic winds off the coast account for about 87% of the actual winds at the 925-hPa level. From our two terrain sensitivity experiments (NoTW and LowFJ), it is apparent that the orographic effects (blocking) of the Taiwan and Fujian terrain only play a secondary role in the development of the CBLJ.

The CBLJ has a nocturnal maximum, though its geostrophic wind component is faster in the afternoon. Easterly ageostrophic winds develop at low levels in the afternoon as a result of a thermally driven circulation arising from a land–sea thermal contrast. After sunset, the easterly ageostrophic winds offshore rotate clockwise and become southerly ageostrophic winds at night. The southerly ageostrophic winds at night plus southerly geostrophic winds are responsible for the nocturnal CBLJ maximum. From the momentum balance, the Coriolis force acting on the ageostrophic winds is found to be the main mechanism for the diurnal variations of the CBLJs. A NoFlux sensitivity experiment shows that the thermally driven circulation near the coast is the main cause for the simulated low-level ageostrophic winds toward the coast in the afternoon hours. In the NoFlux experiment, the ageostrophic winds become much weaker due to the absence of a diurnal thermally driven circulation. Furthermore, the orographic effect by the terrain of Taiwan and Fujian are more significant with a slightly larger (~1 $\mathrm{m\,s^{-1}}$) southerly wind component north of the Taiwan Strait at night than in the afternoon hours, which also partially contributes to the simulated nocturnal maximum in the CBLJ.

Acknowledgments. This study is supported by the Chinese 973 Program 2013CB430104 and the Chinese National Science Foundation under Grants 40921160380, 4141101075, and 41330421. The lead author gratefully acknowledges the financial support of the China

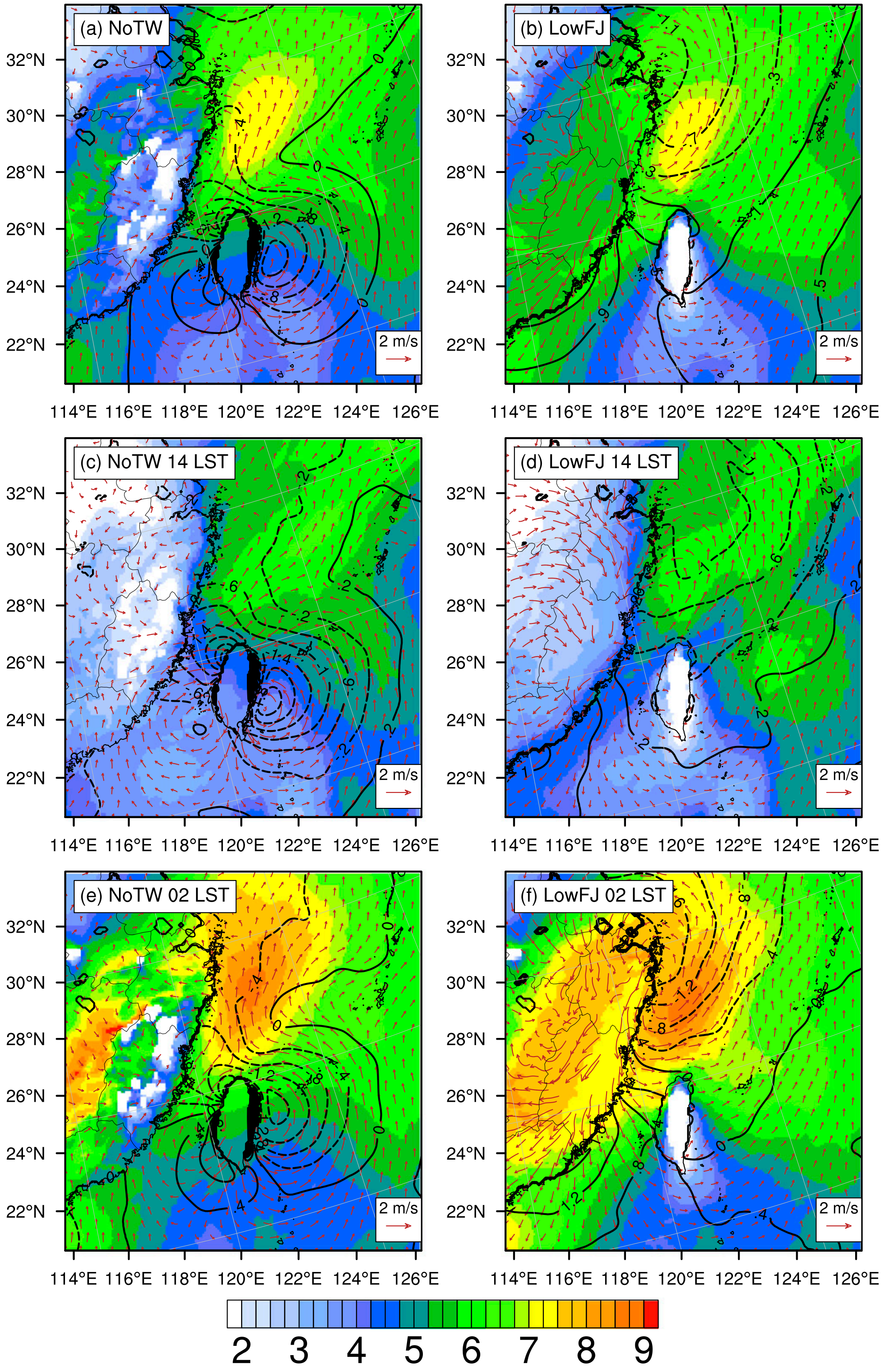

FIG. 18. The simulated differences in wind vectors and geopotential height [solid (dashed) lines denote positive (negative); interval 0.4 gpm] (a),(c),(e) between the REAL and NoTW experiments and (b),(d),(f) between the REAL and LowFJ experiments for (top to bottom) the daily mean, 1400 LST, and 0200 LST for July 2006–11. Wind speed ($\mathrm{m\,s^{-1}}$) is denoted by shading.

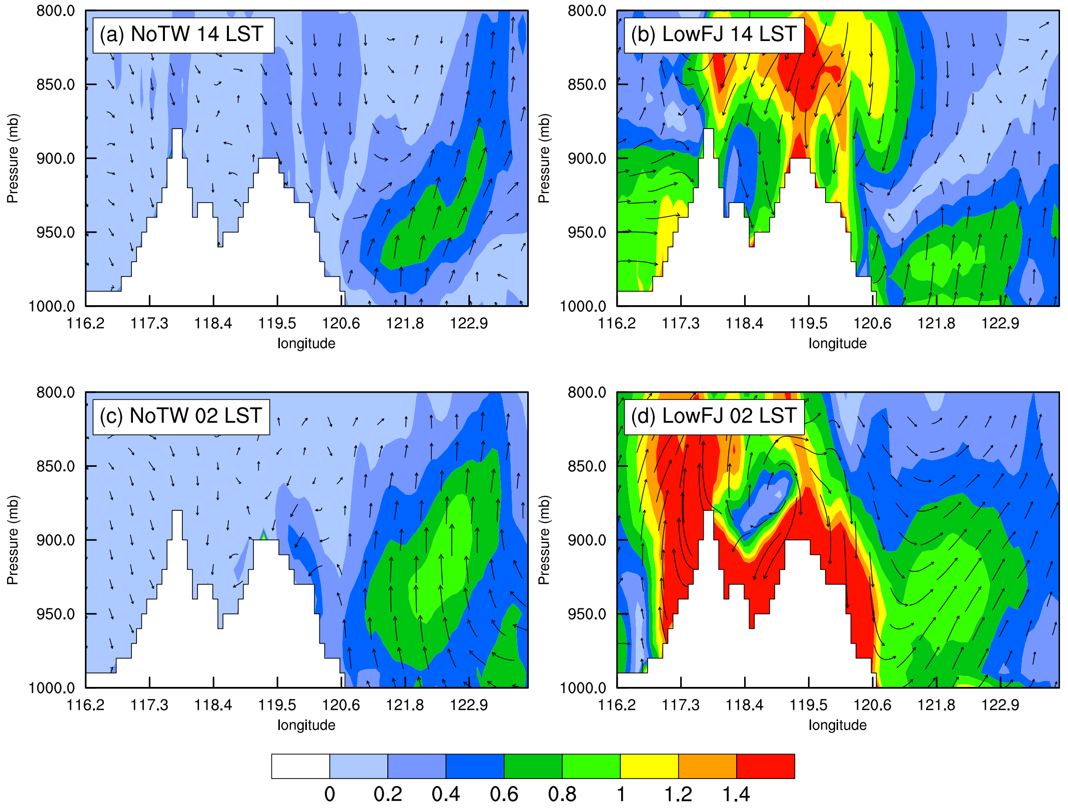

FIG. 19. Longitude–pressure cross sections of simulated differences in wind vectors and the mean horizontal winds (a),(c) between the REAL and NoTW experiments and (b),(d) between the REAL and LowFJ experiments for (top) 1400 and (bottom) 0200 LST along the black line in Fig. 1a for July 2006–11. Shading denotes wind speed differences. Wind vectors denote horizontal wind differences (e.g., upward means southerly wind difference).

Scholarship Council for his visit to the University of Hawai‘i at Mānoa (UHM). Part of the computing resources was funded by the U.S. National Science Foundation to UHM under Grant AGS-1142558. The authors are thankful to Chuan-Kai Wang and Chih-Ying Chen for their assistance, and May Izumi for editing the text.

REFERENCES

Blackadar, A. K., 1957: Boundary layer wind maxima and their significance for the growth of nocturnal inversions. *Bull. Amer. Meteor. Soc.,* **38,** 283–290.

Bonner, W. D., 1968: Climatology of the low level jet. *Mon. Wea. Rev.,* **96,** 833–850, doi:10.1175/1520-0493(1968)096<0833:COTLLJ>2.0.CO;2.

Burk, S. D., and W. T. Thompson, 1996: The summertime low-level jet and marine boundary layer structure along the California coast. *Mon. Wea. Rev.,* **124,** 668–686, doi:10.1175/1520-0493(1996)124<0668:TSLLJA>2.0.CO;2.

Chakraborty, A., R. S. Nanjundiah, and J. Srinivasan, 2009: Impact of African orography and the Indian summer monsoon on the low-level Somali jet. *Int. J. Climatol.,* **29,** 983–992, doi:10.1002/joc.1720.

Colle, B. A., and D. R. Novak, 2010: The New York Bight jet: Climatology and dynamical evolution. *Mon. Wea. Rev.,* **138,** 2385–2404, doi:10.1175/2009MWR3231.1.

Doyle, J. D., and T. T. Warner, 1993: A three-dimensional investigation of a Carolina low-level jet during GALE IOP 2. *Mon. Wea. Rev.,* **121,** 1030–1047, doi:10.1175/1520-0493(1993)121<1030:ATDNIO>2.0.CO;2.

Drobinski, P., R. Rotunno, and T. Dubos, 2011: Linear theory of the sea breeze in a thermal wind. *Quart. J. Roy. Meteor. Soc.,* **137,** 1602–1609, doi:10.1002/qj.847.

Du, Y., and R. Rotunno, 2014: A simple analytical model of the nocturnal low-level jet over the Great Plains of the United States. *J. Atmos. Sci.,* **71,** 3674–3683, doi:10.1175/JAS-D-14-0060.1.

——, Q. H. Zhang, Y. Yue, and Y. M. Yang, 2012: Characteristics of low-level jets in Shanghai during the 2008–2009 warm seasons as inferred from wind profiler radar data. *J. Meteor. Soc. Japan,* **90,** 891–903, doi:10.2151/jmsj.2012-603.

——, ——, Y. L. Chen, Y. Y. Zhao, and X. Wang, 2014: Numerical simulations of spatial distributions and diurnal variations of low-level jets in China during early summer. *J. Climate,* **27,** 5747–5767, doi:10.1175/JCLI-D-13-00571.1.

Garreaud, R., and C. M. Ricardo, 2005: The low-level jet off the west coast of subtropical South America: Structure and variability. *Mon. Wea. Rev.,* **133,** 2246–2261, doi:10.1175/MWR2972.1.

Haurwitz, B., 1947: Comments on the sea-breeze circulation. *J. Meteor.,* **4,** 1–8, doi:10.1175/1520-0469(1947)004<0001:COTSBC>2.0.CO;2.

Jiang, Q., S. Wang, and L. O’Neill, 2010: Some insights into the characteristics and dynamics of the Chilean low-level coastal jet. *Mon. Wea. Rev.,* **138,** 3185–3206, doi:10.1175/2010MWR3368.1.

Jiménez, P. A., J. F. González-Rouco, E. García-Bustamante, J. Navarro, J. P. Montávez, J. V.-G. de Arellano, J. Dudhia, and A. Muñoz-Roldan, 2010: Surface wind regionalization over complex terrain: Evaluation and analysis of a high-resolution WRF simulation. *J. Appl. Meteor. Climatol.,* **49,** 268–287, doi:10.1175/2009JAMC2175.1.

Krishnamurti, T. N., J. Molinari, and H. L. Pan, 1976: Numerical simulation of the Somali jet. *J. Atmos. Sci.,* **33,** 2350–2362, doi:10.1175/1520-0469(1976)033<2350:NSOTSJ>2.0.CO;2.

Li, J., and Y. L. Chen, 1998: Barrier jets during TAMEX. *Mon. Wea. Rev.,* **126,** 959–971, doi:10.1175/1520-0493(1998)126<0959:BJDT>2.0.CO;2.

Lin, P.-L., Y.-L. Chen, C.-S. Chen, C.-L. Liu, and C.-Y. Chen, 2011: Numerical experiments investigating the orographic effects on a heavy rainfall event over the northwestern coast of Taiwan during TAMEX IOP 13. *Meteor. Atmos. Phys.,* **114,** 35–50, doi:10.1007/s00703-011-0155-7.

Lo, J. C.-F., Z.-L. Yang, and R. A. Pielke Sr., 2008: Assessment of three dynamical climate downscaling methods using the Weather Research and Forecasting (WRF) model. *J. Geophys. Res.,* **113,** D09112, doi:10.1029/2007JD009216.

Novak, D. R., and B. A. Colle, 2006: Observations of multiple sea breeze boundaries during an unseasonably warm day in metropolitan New York City. *Bull. Amer. Meteor. Soc.,* **87,** 169–174, doi:10.1175/BAMS-87-2-169.

Parish, T. R., and L. D. Oolman, 2010: On the role of sloping terrain in the forcing of the Great Plains low-level jet. *J. Atmos. Sci.,* **67,** 2690–2699, doi:10.1175/2010JAS3368.1.

Pomeroy, K. R., and T. R. Parish, 2001: A case study of the interaction of the summertime coastal jet with the California topography. *Mon. Wea. Rev.,* **129,** 530–539, doi:10.1175/1520-0493(2001)129<0530:ACSOTI>2.0.CO;2.

Ranjha, R., G. Svensson, M. Tjernström, and A. Semedo, 2013: Global distribution and seasonal variability of coastal low-level jets derived from ERA-Interim reanalysis. *Tellus,* **65A,** 20412, doi:10.3402/tellusa.v65i0.20412.

Rife, D. L., J. O. Pinto, A. J. Monaghan, C. A. Davis, and J. R. Hannan, 2010: Global distribution and characteristics of diurnally varying low-level jets. *J. Climate,* **23,** 5041–5064, doi:10.1175/2010JCLI3514.1.

Rotunno, R., 1983: On the linear theory of the land and sea breeze. *J. Atmos. Sci.,* **40,** 1999–2009, doi:10.1175/1520-0469(1983)040<1999:OTLTOT>2.0.CO;2.

Saha, S., and Coauthors, 2010: The NCEP Climate Forecast System Reanalysis. *Bull. Amer. Meteor. Soc.,* **91,** 1015–1057, doi:10.1175/2010BAMS3001.1.

Schmidt, F. H., 1947: An elementary theory of the land-and sea-breeze circulation. *J. Meteor.,* **4,** 9–20, doi:10.1175/1520-0469(1947)004<0009:AETOTL>2.0.CO;2.

Sjostedt, D. W., J. T. Sigmon, and S. J. Colucci, 1990: The Carolina nocturnal low-level jet: Synoptic climatology and a case study. *Wea. Forecasting,* **5,** 404–415, doi:10.1175/1520-0434(1990)005<0404:TCNLLJ>2.0.CO;2.

Song, J., K. Liao, R. L. Coulter, and B. M. Lesht, 2005: Climatology of the low-level jet at the Southern Great Plains atmospheric boundary layer experiments site. *J. Appl. Meteor.,* **44,** 1593–1606, doi:10.1175/JAM2294.1.

Stensrud, D. J., 1996: Importance of low-level jets to climate: A review. *J. Climate,* **9,** 1698–1711, doi:10.1175/1520-0442(1996)009<1698:IOLLJT>2.0.CO;2.

Yang, Y., Y.-L. Chen, and F. M. Fujioka, 2005: Numerical simulations of the island-induced circulation over the island of Hawaii during HaRP. *Mon. Wea. Rev.,* **133,** 3693–3713, doi:10.1175/MWR3053.1.

Žagar, N., M. Žagar, J. Cedilnik, G. Gregorič, and J. Rakovec, 2006: Validation of mesoscale low-level winds obtained by dynamical downscaling of ERA40 over complex terrain. *Tellus,* **58A,** 445–455, doi:10.1111/j.1600-0870.2006.00186.x.

Zemba, J., and C. A. Friehe, 1987: The marine atmospheric boundary layer jet in the Coastal Ocean Dynamics Experiment. *J. Geophys. Res.,* **92,** 1489–1496, doi:10.1029/JC092iC02p01489.

Zhang, D. L., S. Zhang, and S. J. Weaver, 2006: Low-level jets over the mid-Atlantic states: Warm-season climatology and a case study. *J. Appl. Meteor. Climatol.,* **45,** 194–209, doi:10.1175/JAM2313.1.

Zhang, J. P., and Coauthors, 2012: The impact of circulation patterns on regional transport pathways and air quality over Beijing and its surroundings. *Atmos. Chem. Phys.,* **12,** 5031–5053, doi:10.5194/acp-12-5031-2012.